AAS 17-599

OPTICAL-BASED KINEMATIC POSITIONING FOR DEEP-SPACE NAVIGATION

Stephen B. Broschart[*], Nicholas Bradley[*], and Shyam Bhaskaran[†]

NASA's Deep Space 1 mission demonstrated that a spacecraft can be navigated autonomously during deep-space cruise operations using only images of distant asteroids as measurements. This paper derives an approximation of the position estimate accuracy that can be achieved with this technique based on the assumption of multiple, simultaneous line-of-sight measurements. This achievable accuracy is computed for locations across the solar system, which can be used to estimate cruise navigation performance as a function of spacecraft trajectory. It is shown that a on-board optical navigation system can achieve kinematic position estimate accuracies of better than 100 km throughout the inner solar system with a high-performance camera and from many hundred to several thousand kilometers with a low-end camera. Beyond the main-asteroid belt, the feasibilty of this approach suffers due to lack of targets. A case-study implementation of this approach for the upcoming InSight mission to Mars is also presented.

INTRODUCTION

Deep space navigation techniques have evolved over the past 50 years, steadily improving performance such that remarkable accuracies are achievable in delivering spacecraft to their intended targets for a wide range of missions. The standard technique common to all interplanetary missions uses radiometric data from the spacecraft to determine the spacecraft's orbit and, when needed, perform maneuvers to correct the orbit. The radiometric data includes two-way Doppler and range, which measure the line-of-sight velocity and distance of the spacecraft relative to a tracking station, respectively. Another data type, Delta-Differential One-way Range (DDOR) is an interferometric method which uses the delay of the transmitted signal from two widely-separated stations to determine the angular position of the spacecraft relative to the baseline of the two stations. Finally, for some missions, an onboard camera is used to image a natural body against the star background to obtain a target-relative angular measurement. This Optical Navigation data (OpNav) is especially useful when the orbit of the target body is poorly known, which is typical for asteroids, comets, and planetary satellites.

For almost all past missions, the measurement data are processed on the ground to compute the orbit and maneuvers, then commands are uplinked to the spacecraft. While this approach has been very successful, it has the drawback that maneuvers are executed based on measurements that are

[*]Outer Planet Navigation Group, Mission Design and Navigation Section, Jet Propulsion Laboratory, California Institute of Technology. 4800 Oak Grove Drive, Pasadena, California, 91109.

[†]Group Supervisor, Outer Planet Navigation Group, Mission Design and Navigation Section, Jet Propulsion Laboratory, California Institute of Technology. 4800 Oak Grove Drive, Pasadena, California, 91109.

©2017 California Institute of Technology. Government sponsorship acknowledged.

on the order of a couple of days old. This gap between the last measurement time and maneuver execution includes the time for data to travel from the spacecraft to the ground and be processed, time to formulate, test, and approve a response, and the time to send the response command back to the spacecraft. During this period, the spacecraft is diverging from the estimated orbit, which limits how accurately the spacecraft can be navigated. Another drawback is that the standard approach requires a dedicated Deep Space Network (DSN), or equivalent, antenna to be reserved for both the downlink of the measurement data and the uplink of commands. Given the increasing number and ambitions of space missions, it will become increasingly difficult to meet navigation requirements and to provide the necessary radiometric tracking infrastructure needed to support all missions. A spacecraft that can perform its own navigation using a self-contained system would avoid the limitations above, enabling rapid turnaround of late-breaking measurements to improve navigation performance and free up antenna time at ground-based tracking stations. These improved capabilities would allow for more numerous and more ambitious missions, resulting in improved science yield.

One approach to on-board navigation is to use on-board imagery of distant known asteroids and other bodies to effectively triangulate the spacecraft position. This concept was actually implemented as part of the AutoNav on-board navigation system on NASA's Deep Space 1 mission (DS1).[1–3] During July and August of 1999, DS1 autonomously navigated a cruise trajectory in the inner solar system using only images of asteroids chosen from a list of around 5,000 known at that time. Intiution may suggest that asteroids are too dim to be seen reliably from a spacecraft, but in fact many can be imaged from positions throughout the inner solar system with a relatively modest space-rated camera. In fact, asteroids are ideal observation candidates for navigation because they lack atmospheres that degrades center-finding accuracy for planetary bodies and the orbits of individual asteroids are almost completely uncorrelated from each other. Also, asteroids are evenly distributed longitudinally around the Sun, so the availability of targets does not depend significantly on timing. As of 2017, around 500,000 asteroids have ephemerides that are known to better than 500 km,[4] which usually provides plenty of targets for accurate inertial triangulation and generally avoids the need for image mosaicing.

In this paper, the autonomous navigation strategy of DS1 is considered broadly to assess the extensibility of the concept for missions throughout the solar system. First, results are presented that show how many asteroids can be seen at varying locations throughout the solar system for a representative selection of camera implementations. Next, an analytical formulation is derived to compute the uncertainty associated with a kinematic estimate of spacecraft position based on multiple simultaneous asteroid images. This upper bound for expected navigation uncertainty is computed for locations throughout the solar system. Finally, this optical-only technique is applied in simulation to the InSight transfer from Earth to Mars and compared against the mission's baseline radiometric approach to give an example of the achievable navigation performance.

Previous Studies and Contributions

In addition to the DS1 work, a number of paper studies have been done that estimate the performance of an autonomous navigation system using only OpNav measurements in various contexts. Tuckness *et al.* proposed two filter strategies for navigating a transfer trajectory from the Earth to the Moon using only OpNav observations of the Earth, Moon, and Sun.[5] Long *et al.* considered navigation of a high-Earth orbiter using only OpNav observations of the Earth and Sun.[6] Vasile *et al.* went beyond the Earth-Moon system to do a simulation of cruise trajectories from Earth to Mer-

cury and Earth to Jupiter using asteroids as targets for the OpNav measurements.[7] Ceccarelli *et al.* also did a simulation of a transfer from the Earth to the Moon using only OpNav observables of the Moon.[8] Zanetti studied the notion of an on-board OpNav system being used as a backup navigation system to support the Orion spacecraft return trajectories from the Moon using measurements of the Earth's horizon[9] and Llop recently presented simulation results for an autonomous navigation system operating in a Earth-Moon halo orbit using measurements of the Moon's angular extent.[10] Finally, recent results from Kawabata *et al.* and Segret *et al.* have examined triangulation in deep space in a limited way.[11,12]

This paper makes several unique contributions. First, the analytical formulations for the kinematic triangulation accuracy and the target-selection heuristics have not been presented elsewhere. These contributions facilitate a solar-system-wide characterization of the position estimate accuracy that can be achieved, which contrasts with the analysis of individual trajectories presented previously. The formulation here is also the first to include the effects of target body uncertainties systematically in the accuracy assessment. Finally, a realistic case-study application of the approach is presented, which is unique in that it focuses on the quantities that are mission requirements (e.g., fuel cost and navigation delivery to the target) instead of just spacecraft trajectory estimate accuracy. While far from conclusive, the case study illustrates some of the complex tradeoffs between optical and radiometric navigation approaches.

Finally, it should be noted that mathematics of orbit estimation using line-of-sight (LOS) measurements have been studied extensively in papers treating very similar problems to on-board deep-space navigation. The interested reader may find additional insight into the problem presented here through study of the literature on "angles-only" orbit determination related to planetary and asteroid ephemeris estimation, on-orbit rendezvous using OpNav measurements, and terrain-relative navigation.

MODELING AND ASSUMPTIONS

Target Database

The database of potential observation targets used here, $\mathbf{T_{all}}$,* consists of the eight planets, 49,607 asteroids with absolute magnitude less than 14.7, Ceres, Pluto, the Moon, Phobos, Deimos, the four Galilean moons of Jupiter, and the six largest moons of Saturn. The Horizons database maintained by JPL's Solar System Dynamics group (JPL-SSD) provides the asteroid locations and corresponding formal uncertainties.[4] All of the included targets have well-characterized orbits, indicated by a "condition code" of zero in the Horizons database. The planet and moon locations are obtained from the DE430, MAR097, JUP310, and SAT375 ephemerides, provided by the JPL NAIF system.[13] The planet and moon ephemeris uncertainties are approximated as Cartesian spherically-symmetric, based on the magnitude of their formal state uncertainties. All target ephemeris uncertainties are assumed to be independent (i.e. uncorrelated), except for the orbits of the moons around their respective planets.

Fig. 1 (left) shows the distribution of semi-major axes across all of the candidate targets, grouped by absolute magnitude. The vast majority of targets are in either the main-asteroid belt between Mars and Jupiter ($\sim$2-4 AU), or in the Trojan and Greek populations that co-orbit the Sun with Jupiter ($\sim$5 AU). Fig. 1 (right) shows the distribution of formal position uncertainties (at epoch) for

*A nomenclature table is provided at the end of the document.

the asteroids in the target database. A typical asteroid in the database has a maximum 1-σ position uncertainty of less than $\sim$100 km and almost all of the brighter targets have less than 200 km.

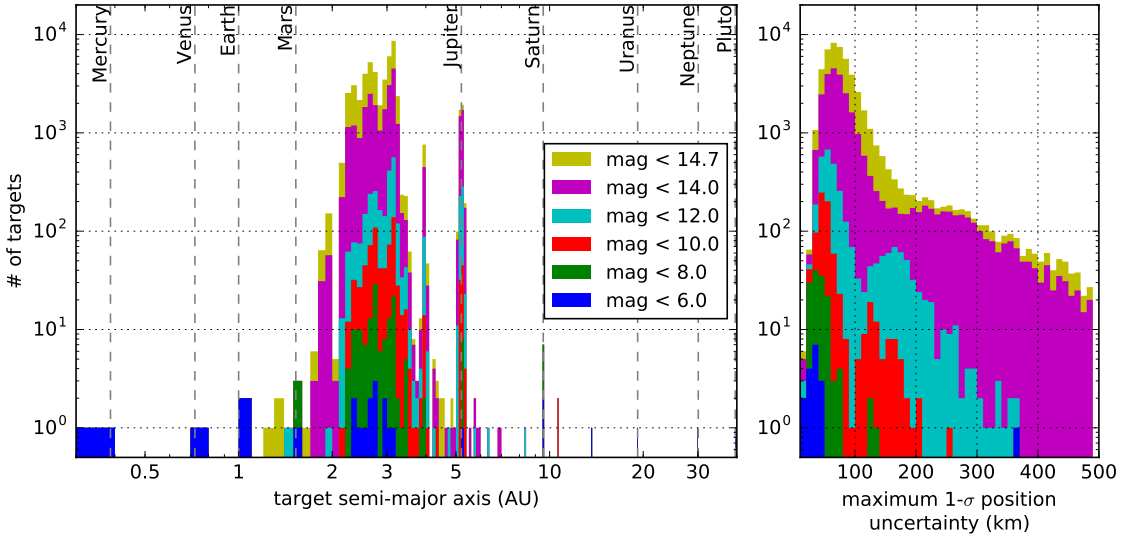

Figure 1. Histogram of candidate target semi-major axes (left) and orbit position uncertainties (right). Color indicates absolute magnitude.

Camera Performance

The three representative camera implementations used for generating results are given in Table 1, where FOV is the camera field-of-view, Θ is the field-of-view of one camera pixel (typically known as the "instantaneous field-of-view" or IFOV), M_{max} is the maximum visible apparent magnitude, and ψ_{min} is the minimum allowable Sun-spacecraft-target angle. FOV and Θ are fixed geometric parameters solely based on the choice of camera. ψ_{min} may depend on how the camera is mounted on the spacecraft, and how it may be baffled.* M_{max} depends on the pointing stability the spacecraft can provide, exposure time, and the image processing techniques used.

Table 1. Spacecraft-camera performance parameters

Name	FOV (deg)	Θ (μrad)	M_{max}	ψ_{min} (deg)
Low Res	26.9	128.0	9.5	30
Mid Res	7.0	60.0	10.5	30
Hi Res	0.6	10.0	13.5	30

The parameters in Table 1 are chosen to be representative of the range of camera performance available to current space missions, with the "Low Res" option representing the CubeSat end of the spectrum and the "Hi Res" option representing a very high quality science camera implementation.

Observations

The measurement observables are the sample and line coordinates of the target body center-of-mass as viewed by the spacecraft camera. Computed values of these observables are predicted based

*Though a constant value is assumed here, ψ_{min} may vary weakly with distance from the Sun.

on the camera parameters, spacecraft attitude, and direction to the target.[14] For the purpose of this study, a simplified form of the sample and line observables under the gnomonic projection is used,

$$\left[\begin{array}{c} s \\ l \end{array} \right] = \frac{1}{\Theta \delta r^C_{b,z}} \left[\begin{array}{c} \delta r^C_{b,x} \\ \delta r^C_{b,y} \end{array} \right], \tag{1}$$

where $\delta \tilde{\mathbf{r}}^C_b = \left[\begin{array}{ccc} \delta r^C_{b,x}, & \delta r^C_{b,y}, & \delta r^C_{b,z} \end{array} \right]^T = \mathbf{C}^T \delta \tilde{\mathbf{r}}_b$ is the position of the target relative to the spacecraft in the camera frame, $\delta \tilde{\mathbf{r}}_b$ is the inertial position of the target relative to the spacecraft, and $\mathbf{C}$ is the rotation matrix from the inertial frame to the camera frame. This formulation ignores camera distortion and simplifies the detector geometry without any loss of generality.*

It is assumed that an image processing scheme exists that can localize the target center-of-mass in an image† to a 1-σ accuracy of 0.25 camera pixels, i.e., $\sigma_{cf} = 0.25\Theta$. This performance is consistent with what is typically possible with current standard techniques for observations of point sources. The observables are real valued and not restricted to integer pixel numbers, even when the target spans less than 1 camera pixel, since the observable can be interpolated from the light that is spread over the adjacent pixels. The only other contribution to the measurement uncertainty model used here is the uncertainty in the target body ephemeris. It is assumed that at least three background stars are visible in each image, which can be used to solve for the inertial camera pointing to a neglible level of error. It is also assumed that the camera has been calibrated so as to reduce unmodeled optical distortions to negligible levels, and the ratio of the distance to the targeted bodies to the spacecraft velocity is large enough so that image time tag errors are also negligible.

TARGET VISIBILITY

The feasibility of onboard autonomous navigation relies upon the ability to generate observables of enough targets to triangulate the spacecraft position. To create a quality observable, the signal-to-noise ratio of the target against the image background noise must be sufficient. Here, a comparison of the target's apparent magnitude M (Eq. (2)) against the capability of the spacecraft-camera combination (modeled using M_{max}) is used to determine which targets from the database can be imaged as a function of spacecraft position.

For a given spacecraft $\tilde{\mathbf{r}}_{sc}$ and target position $\tilde{\mathbf{r}}_b$ the apparent magnitude of a target b is computed as

$$M\left(\tilde{\mathbf{r}}_b, \tilde{\mathbf{r}}_{sc}\right) = H + 5\log_{10}\left(\frac{||\delta\tilde{\mathbf{r}}_b||\,||\tilde{\mathbf{r}}_b||}{AU^2}\right) - 2.5\log_{10}\left(\phi_1\right), \tag{2}$$

where

$$\phi_1 = \left(\sin\left(\phi\right) + \left(\pi - \phi\right)\cos\left(\phi\right)\right)/\pi \tag{3}$$

is the phase function and ϕ is the Sun-target-spacecraft angle. For a given spacecraft position, M_{max}, and time, the set of visible asteroids is defined as

$$\mathbf{T}_{visible}\left(t, \tilde{\mathbf{r}}_{sc}, M_{max}\right) = \{b \in \mathbf{T}_{all} : M\left(\tilde{\mathbf{r}}_b\left(t\right), \tilde{\mathbf{r}}_{sc}\right) <= M_{max} \wedge \psi > \psi_{min}\}, \tag{4}$$

where ψ is the Sun-spacecraft-target angle.

*For full formulation see Reference 14

†This requires assumptions on the target body shape and phase function to correct for the center-of-brightness to center-of-mass offset. When the diameter of the target body is significantly less than 1 pixel, the error arising from reasonable assumptions about the body's reflective properties is not significant to the analysis presented here.

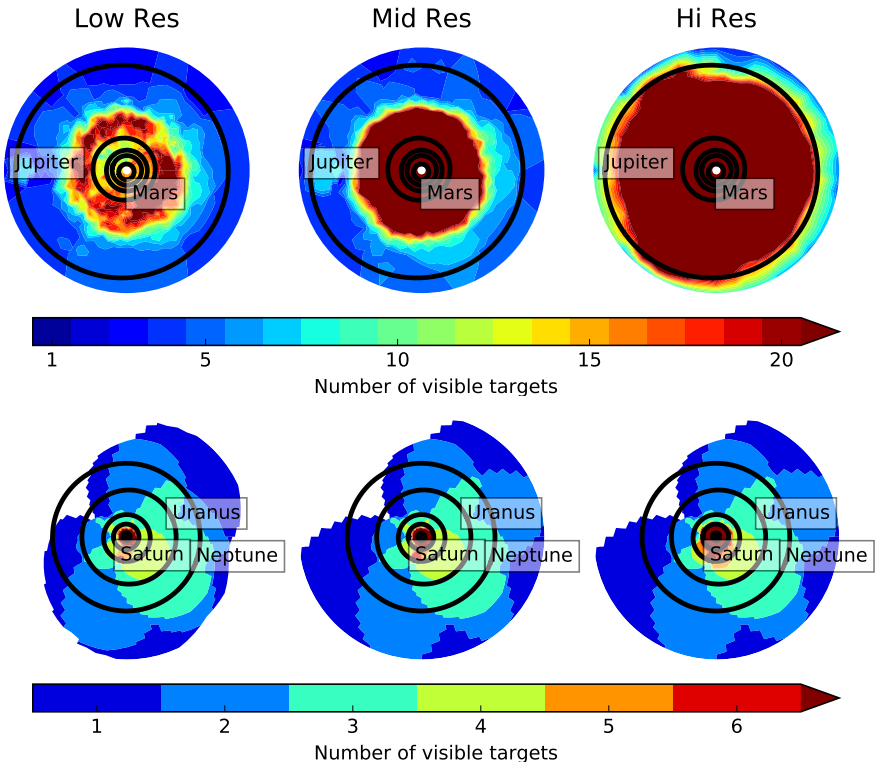

Figure 2. Number of targets visible inside 6 AU (top) and inside 35 AU (bottom) for each camera on July 31, 2016.

Figs. 2 (top) and 2 (bottom) show the number of visible targets from the database in the inner and outer solar system, respectively, using each of the cameras in Table 1 at an arbitrarily-chosen time. Even for the Low Res camera, at least a dozen targets are generally visible within or inside of the main-asteroid belt. The Mid Res camera provides between 20 and 50 targets throughout this same part of the solar system and the Hi Res can typically see between 300 and 500 targets. Given the large number and homogeneous spatial distribution of asteroids in the main-asteroid belt, these results should not change qualitatively for different epochs. Beyond the main-asteroid belt, significantly fewer targets are visible and the feasibility of optical triangulation is primarily dependent on the relative positions of the outer planets. The main-belt asteroids also become dimmer as ϕ increases, and they are eventually omitted by the ψ_{min} constraint.

Only two observations are needed to triangulate the spacecraft position, so the results in Fig. 2 show that it is mathematically feasible to generate an instantaneous estimate (of some accuracy) of spacecraft position using only on-board measurements for any location inside of Jupiter's orbit, even with a relatively low-performance camera. Further, there are many more observations possible inside of the outer-edge of the main-asteroid belt, which allows for improved accuracy, robustness against bad measurements, and more choices to address spacecraft-specific constraints. In the outer solar system, the autonomous navigation approach is less promising due to a scarcity of targets. The feasibility would likely need to be studied on a case-by-case mission basis. It may also be possible that the results could be improved by including the Centaur objects (minor planets in the outer solar system) in the database. These objects are excluded here due to insufficiently characterized orbits.

KINEMATIC POSITION UNCERTAINTY

A general impression of the navigation accuracy that can be achieved using on-board optical measurements for a particular mission can be gained by looking at the position uncertainty that can be achieved instantaneously with several simultaneous measurements at locations along the spacecraft trajectory. This approach creates a result that is more conservative than would be achieved by combining the information from the same observations over time in a navigation filter, but the advantage is that the kinematic accuracy is simpler to compute and extend across different scenarios.

The assumption that multiple measurements can be made simultaneously only strictly holds when the camera FOV is wide enough to image multiple targets simultaneously. However, if it were necessary for the spacecraft to slew between images over a finite period of time, the position estimate accuracy produced by a navigation filter would not meaningfully change since the change in $\delta\tilde{\mathbf{r}}_b$ would be well predicted over a short period of time.

Formulation

For the scenario where the spacecraft position is estimated with the target body position included as a consider parameter, the formulation of the covariance matrix P_c takes the typical form,[15]

$$\mathbf{P}_c = \begin{bmatrix} \mathbf{P}_{xx}, & \mathbf{P}_{xc} \\ \mathbf{P}_{xc}, & \bar{\mathbf{P}}_{cc} \end{bmatrix} = (\Lambda)^{-1}, \tag{5}$$

where P_{xx} is the kinematic position uncertainty, $\bar{P}_{cc}$ is the *a priori* covariance for the target body position, and P_{xc} is the cross-correlation. Λ is the information matrix,

$$\Lambda = \sum_{b \in \mathbf{T^n_{obs}}} \Lambda_b = \sum_{b \in \mathbf{T^n_{obs}}} \begin{bmatrix} \mathbf{H}_{x,b}^\top \mathbf{R}^{-1} \mathbf{H}_{x,b}, & \mathbf{H}_{x,b}^\top \mathbf{R}^{-1} \mathbf{H}_{c,b} \\ \mathbf{H}_{c,b}^\top \mathbf{R}^{-1} \mathbf{H}_{x,b}, & \mathbf{H}_{c,b}^\top \mathbf{R}^{-1} \mathbf{H}_{c,b} + \bar{\mathbf{P}}_{cc} \end{bmatrix}, \tag{6}$$

which is the sum of the independent contribution Λ_b from the observation of each target and $\mathbf{T^n_{obs}}$ is the set of n observed targets. $\mathbf{H}_{x,b}$ is the 2×3 Jacobian matrix that contains the partial derivatives of the sample and line observable of target b (Eq. (1)) with respect to the spacecraft position. Similarly, $\mathbf{H}_{c,b}$ contains the partial derivatives of the observables with respect to the positions of all of the target bodies (2×3n).* $\mathbf{R}$ is the 2×2 measurement covariance matrix, which is assumed here to be $\sigma_{cf}^2 \mathbf{I}_{2\times 2}$ (uncorrelated). The Jacobian matrices are computed as

$$\mathbf{H}_{x,b} = -\frac{1}{\Theta \delta r_{b,z}^C} \begin{bmatrix} 1, & 0, & -\delta r_{b,x}^C / \delta r_{b,z}^C \\ 0, & 1, & -\delta r_{b,y}^C / \delta r_{b,z}^C \end{bmatrix} \mathbf{C} \tag{7}$$

and

$$\mathbf{H}_{c,b} = -\mathbf{H}_{x,b}. \tag{8}$$

Scalar Metric

For the purpose of succinctly representing the 3×3 kinematic spacecraft position estimate uncertainty, $\mathbf{P}_{xx}$ can be reduced to the root-sum-of-squares (RSS) of the individual coordinate uncertainties, σ_{pos}, using Eq. (9),

$$\sigma_{pos}\left(\delta\tilde{\mathbf{r}}_1, ..., \delta\tilde{\mathbf{r}}_n, \Theta, \sigma_{cf}\right) = \sqrt{tr(\mathbf{P}_{xx})}, \tag{9}$$

*If the targets and spacecraft orbit a different body, then the $\mathbf{H}_{c,b}$ must be expanded to also include the corresponding central bodies.

where $tr()$ is the trace operator. σ_{pos} is a conservative estimate of uncertainty that is always between 1 and $\sqrt{3}$ times the maximum 1-σ uncertainty associated with $\mathbf{P}_{xx}$.

If only two observations are used and the consider effect of target body ephemeris uncertainty is ignored, σ_{pos} can be computed exactly in closed form,

$$\sigma_{pos,2}\left(\delta r_1, \delta r_2, \theta, \Theta, \sigma_{cf}\right) = \frac{\sqrt{\delta r_1^4 + \delta r_1^2 \delta r_2^2 \sin^2(\theta) + 2\delta r_1^2 \delta r_2^2 + \delta r_2^4}}{\sin(\theta)\sqrt{\delta r_1^2 + \delta r_2^2}} \Theta \sigma_{cf} \tag{10}$$

where δr_1 and δr_2 are the nominal distances to the two observed targets and θ is the angle between the two observations (see Appendix A).

Equation (10) is helpful to understand how σ_{pos} varies with relative target geometry. If the observations are coaligned, θ goes to zero and σ_{pos} goes to infinity since there is no information along the line-of-sight to the target. Conversely, σ_{pos} achieves a minimum value for a given set of target ranges when $\theta = 90^o$. For a fixed θ, σ_{pos} is the smallest when the targets are close to the spacecraft, which makes sense since the physical position error corresponding to a given angular observation error is smaller at closer range.* Also notable is that $\sigma_{pos,2}$ scales linearly with the camera Θ and the center-finding accuracy and that the geometric contribution is independent of these hardware and algorithm performance parameters. This separation makes it easy to predict the effect of changing any of the $\sigma_{pos,2}$ parameters.

Results

An estimate of the position accuracy for a variety of interplanetary cruise scenarios using only optical observations of distant bodies is made by computing Eq. (9) for σ_{pos} across the solar system.† Figs. 3 (top) and 3 (bottom) show σ_{pos} values calculated across the inner and outer solar system, respectively, using different cameras and a maximum of six targets. In these cases, the "pseudo-target" heuristic is used to select which visible targets to observe (see Appendix B).

In Fig. 3, the spacecraft location relative to the main-asteroid belt is seen to be a key factor in all cases. Given the concentration of large asteroids in this area (Fig. 1), this strong dependency on heliocentric distance is not unexpected. Generally, σ_{pos} is smallest in the main-belt where close targets are abundant, followed by locations inside of the main belt where main-belt targets are visible but farther away, and largest beyond the main-belt where visibility of the main-belt targets is lost due to large phase angles and solar keep-out angle (i.e., ψ_{min}) constraints. In absolute terms, the poorest performing Low Res camera can achieve typical σ_{pos} accuracies of several thousand kilometers inside of Mars' orbit, high hundreds of kilometers in the main belt, and tens of thousands of kilometers out to Jupiter. The Mid Res camera can achieve σ_{pos} accuracies of around 1,000 km inside of Mars' orbit, several hundred kilometers in the main-belt, and around ten thousand kilometers out to Jupiter. The Hi Res camera achieves accuracies of 100 km or less inside of the outer main-asteroid belt and up to 1,000 km at Jupiter's orbit. Qualitatively, the best results are achieved in regions with the most nearby visible asteroids.

In the outer solar system, Fig. 3 (bottom) shows that the lack of visible targets and the large distances between them result in significantly poorer results than seen in the inner solar system.

*When target ephemeris uncertainty is included, there is a non-zero optimal range for targets that is a function of target ephemeris uncertainty.

†Light time corrections to the apparent positions of the target bodies are not included here to simplify the calculations since the small geometric correction is insignificant to these results.

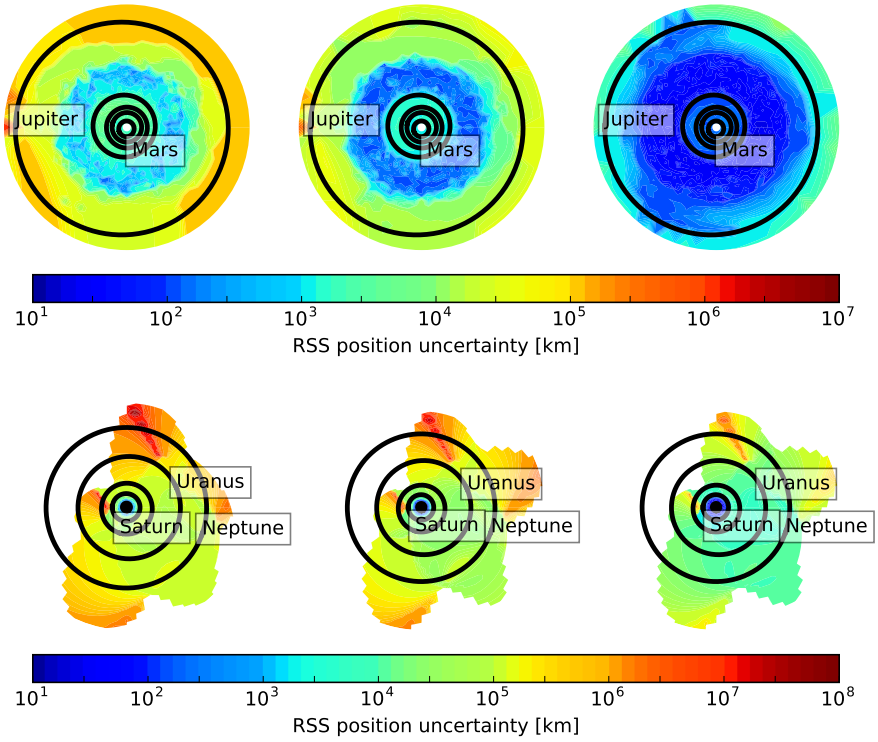

Figure 3. Kinematic RSS position accuracy (σ_{pos}, km) achievable with each camera inside 6 AU (top) and inside 35 AU (bottom) on July 31, 2016. Up to six target bodies are used ($n \leq 6$), though typically no more than 2-4 targets are visible beyond the orbit of Jupiter (see Fig. 2 (bottom)). Areas without color have one or less visible targets and 3-D kinematic positioning cannot be achieved.

To make a kinematic position estimate, at least two observations are necessary and it can be seen in Fig. 2 that many locations do not allow for that. When kinematic solutions are available, the σ_{pos} values range from around 10,000 km with the best camera in the best situations up to tens of millions of kilometers under less ideal circumstances.

IMPLEMENTATION CASE STUDY: THE INSIGHT MISSION TO MARS

In practice, deep space navigation involves not just obtaining instantaneous positions of the spacecraft, but the full trajectory of the spacecraft for the past, present, and predictions into the future. The process used is to perform a linearized least-squares fit to tracking data, estimating corrections to the reference trajectory obtained from numerically integrating the non-linear equations of motion. In addition to estimating the spacecraft state, other parameters which describe the spacecraft motion (e.g., thrusting events, solar radiation pressure), plus biases affecting the data, are also estimated. For a full discussion of the statistical orbit determination process, see Reference 15. An overview of interplanetary navigation techniques can be found in Reference 16.

In order to evaluate the performance of the optical-only approach under a more realistic implementation, the InSight mission to Mars is analyzed here as if the mission were only using on-board optical navigation. The performance for position uncertainty over time, total required $\Delta V99$, B-

Table 2. Planned TCMs for the InSight trajectory to Mars (times are given in Coordinated Universal Time [UTC])

Name	Maneuver Time	DCO (radio)	DCO (optical)
TCM-1	18-JUN-2018 18:00	13-JUN-2018 18:00	18-JUN-2018 17:00
TCM-2	23-JUN-2018 18:00	18-JUN-2018 18:00	23-JUN-2018 17:00
TCAL*	15-JUL-2018 20:10	—	—
TCM-3	12-OCT-2018 18:00	07-OCT-2018 18:00	12-OCT-2018 17:00
TCM-4	11-NOV-2018 18:00	10-NOV-2018 18:00	11-NOV-2018 17:00
TCM-5	18-NOV-2018 18:00	17-NOV-2018 18:00	18-NOV-2018 17:00
TCM-6	25-NOV-2018 21:59	24-NOV-2018 21:59	25-NOV-2018 21:00

* TCAL is an inertially-fixed maneuver. Since it is not designed, it has no data cutoff

Plane delivery accuracy, and entry flight-path angle accuracy are computed and compared against a simulation of the mission's baseline radiometric navigation approach.

Mission Description

The representative InSight trajectory used here launches on June 8, 2018 and follows a 5.5-month Type I transfer trajectory to Mars. The primary navigation goal is to deliver the entry capsule to the Mars atmospheric entry interface point, with a targeted entry flight path angle (EFPA) of -11.99 deg with a 3-σ accuracy no worse than 0.21 deg, which allows safe atmospheric flight for the lander.[17] The second navigation goal is to estimate the EFPA to an accuracy no worse than 0.15 deg (3-σ) at 6 hrs out to initialize the atmospheric flight controller.

The mission plans to use six maneuvers (TCMs) to guide the spacecraft from launch to the Mars atmosphere, whose dates are listed in Table 2. All of the TCMs are nominally zero magnitude and only used to correct navigation errors except for TCM-1, which also has a deterministic component that corrects a planned bias in the launch trajectory. The TCMs all target the atmospheric entry state. The TCAL maneuver design is fixed for thruster calibration purposes and is not used to correct navigation errors.

Simulation Parameters

Two navigation simulations are run for comparison; one that follows the mission's baseline radiometric navigation plan[17] and another that uses only optical measurements. The MONTE software[18] is used to simulate the orbit determination process and to perform the statistical $\Delta V99$ calculation.[19] For the comparison to be as realistic as possible, the MONTE configuration currently used by the InSight ground navigation team was reproduced for this analysis based on code provided by Eric Gustafson at the Jet Propulsion Laboratory*.

In the radiometric case, the mission's baseline filter configuration was used without modification to produce results. To summarize, the estimated parameters in the navigation filter include the spacecraft state at epoch, a fixed bias and stochastic (i.e., time-varying) scale factor on the solar radiation pressure, the ΔV vector of each TCM, and stochastic accelerations in three cartesian components to absorb any dynamic mismodellings and attitude control thrusting. Earth polar motion and spin rate, media calibration errors, tracking station locations, and the Earth and Mars ephemerides are included as consider parameters. Radiometric tracking data starts being collected immediately after

*personal communication, July 2017.

Table 3. Optical data cadence

From (UTC)	To (UTC)	Frequency
11-JUN-2018 17:00	23-JUN-2018 18:00	1 day
25-JUN-2018 20:00	15-JUL-2018 20:10	2 days
19-JUL-2018 17:00	11-NOV-2018 18:00	5 days
14-NOV-2018 17:00	18-NOV-2018 18:00	1 day
18-NOV-2018 20:00	25-NOV-2018 03:00	6 hours
25-NOV-2018 03:00	26-NOV-2018 19:00	1 hour*

* Only Phobos and Deimos are observed during the last time segment

launch and follows the schedule described in the navigation plan.[17] Range, Doppler, and DDOR measurements are used. For the design of each TCM, the data cutoff (DCO) is several days or hours prior to the maneuver to provide time to process the data, estimate the trajectory, design the TCM to correct back to the reference trajectory, and uplink the commands to perform the TCM (See Table 2).

The optical-only case is similar to the radiometric scenario, but replaces all Doppler, Range, and DDOR measurements with on-board optical observations, removes the Earth orientation, media calibrations, and station location consider parameters (since these have no effect on onboard optical data), and moves the DCO times to 1 hr before the corresponding maneuvers since onboard navigation can design the maneuver much more quickly than a ground-based process (see Table 2). Also, the positions for all the targets are added as consider parameters with the uncertainties from the JPL SSD Horizons database.[4] In the case of Phobos and Deimos, approximate radial-transverse-normal (RTN) coordinate 1-σ uncertainties of $[2, 5, 2]$ km and $[3, 5, 3]$ km, respectively, are used. The imaging data starts on June 11, three days after launch, and follows the cadence described in Table 3 thereafter. At each imaging opportunity, up to 10 targets are chosen from the visible asteroids at that time in the target database $\mathbf{T}_{\mathbf{visible}}$ using the pseudo-target heuristic (Eqs. (27) and (29)). Observations of planets and moons are excluded, except in the final set of one-per-hour images when *only* Phobos and Deimos observations are used. The total number of unique asteroids observed over the duration of the cruise was 15, 37, and 36 for the Low Res, Mid Res, and Hi Res cameras, respectively. The data weighting for each observation was set at 0.25 pixels (1-σ).

Simulation Results

Fig. 4 shows the RSS of the position and velocity covariance mapped to the current time at 6 hour intervals for the filter configurations described above. The uncertainties for the radiometric case are considerably smaller for the duration of the cruise, with the radiometric position knowledge largely below 10 km and between 1 and 10 mm/s in velocity. The optical results are always 1 to 3 orders of magnitude worse, depending on the camera, except near the very end where the observations of nearby Phobos and Deimos allow for rapid improvement in the spacecraft state uncertainty.

Aside from remaining within the beam-width of the ground communications station, there is often no mission requirement on the current-state uncertainty during interplanetary cruise (Fig. 4) because it is only indirectly relevant to the mission goals. For an orbiter mission, there is usually a requirement on the accuracy of the delivery to the "B-Plane", which is a plane centered at Mars that is perpendicular to the incoming asymptote of the trajectory.[20] Fig. 5 shows the 3-σ error ellipses mapped from the TCM-6 DCO to the B-Plane for the three optical cases and the radiometric

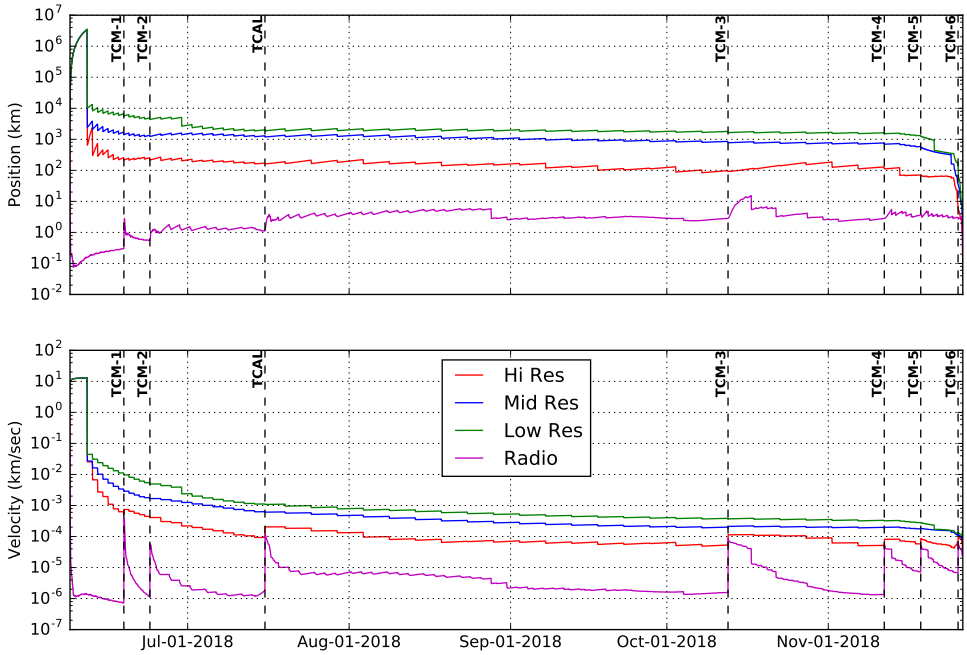

Figure 4. Filtered 3-σ current state knowledge along the InSight trajectory, comparing the results obtained with each of the three cameras against the radio-only case.

case. Since TCM-6 is the last opportunity to correct the trajectory, Fig. 5 effectively shows the expected delivery accuracy to orbit. The elongated ellipse for the radiometric case is typical for Mars approach scenarios. Since the the best measurement accuracy is along the line-of-sight to the Earth, the uncertainty ellipsoid is pancake-shaped. When projected onto the B-Plane (which is aligned with the incoming asymptote), the cross-section is generally elongated. The optical results, however, are nearly circular because the viewing geometry for Phobos and Deimos is always very-nearly perpendicular to the arrival asymptote. Here, the Low and Mid Res cameras delivery performance is considerably worse than the radio result. The Hi Res camera, however, shows considerably better performance at the B-Plane. This is likely to be optimistic, though, because the uncertainty is dominated by Phobos and Deimos observations, which are weighted at point source levels. When these bodies grow to cover more than 1 pixel in the images, the center finding accuracy associated with those observations would likely degrade. In the Linear Time-of-Flight (LTOF) axis, all optical cases have higher uncertainties than the radio. The OpNav observables only an provide indirect measurement of range to the target based on the angular separation of Phobos and Deimos and the distance baseline between them, which is not as powerful as direct range observations.

For a Mars lander mission like InSight, the delivery requirement is defined at the atmospheric entry point. As mentioned above, InSight has a requirement on the EFPA delivery (which is the uncertainty prior to the execution of TCM-6) and a requirement on the accuracy of the post-TCM-6 estimate of the EFPA used to initialize the atmospheric flight control. Table 4 shows the delivery uncertainty at the TCM-6 DCO and the knowledge at 6 hours prior to entry. Recall that the 3-σ delivery and knowledge requirements are 0.21 and 0.15 deg, respectively, which the radiometric case narrowly satisfies. The Hi Res camera result is quite good, easily meeting both requirements.

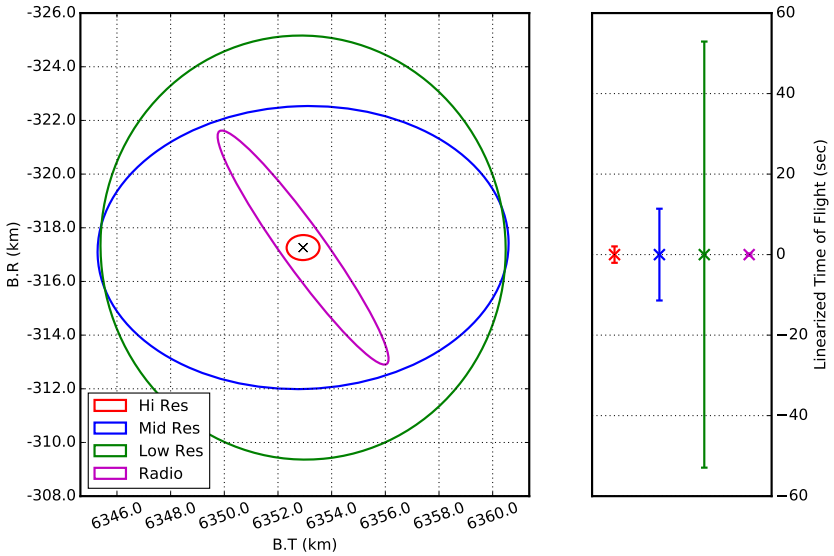

Figure 5. B-Plane 3-σ uncertainty ellipses and Linear-Time-Of-Flight (LTOF) at the TCM6 data cutoff. LTOF uncertainty is shown relative to the nominal LTOF.

Table 4. Entry Flight Path Angle (EFPA) 3-σ uncertainties. The nominal EFPA is -11.99° with a 3-σ requirement of 0.21°.

Data/camera	TCM-6 DCO	Knowledge at Entry - 6 hr
Low Res	0.394°	0.084°
Mid Res	0.408°	0.057°
Hi Res	0.143°	0.012°
Radio only	0.208°	0.100°

The Low and Mid Res cameras do not meet the delivery requirement, but they are quite capable of meeting the knowledge requirement.

One of the direct mission implications of the degraded current-state position uncertainty shown in Fig. 4 is that more fuel may be needed to keep the spacecraft on course. The mass of fuel loaded on-board the spacecraft is based on the $\Delta V99$, which is the amount of velocity correction ability needed to cover 99% of expected navigation dispersions. Table 5 shows the total $\Delta V99$ estimated for the entire mission for the four scenarios. Overall, the $\Delta V99$ result for the Hi Res camera is very comparable to the radiometric result. The Mid Res camera requires a little less than twice the radio case, and the Low Res, a little below a factor of 4. Whether these differences matter or not depends on whether the additional mass for the fuel is acceptable to the mission.

Finally, the amount of DSN tracking required for each scenario can be compared. For the radiometric case, 87 days of 2-way Doppler tracking and 100 DDOR observations are included in

Table 5. ΔV99 for each scenario.

Scenario	Radio-only	Hi Res	Mid Res	Low Res
ΔV99 (m/sec)	11.33	11.48	20.31	40.49

the scenario analyzed. In the optical case, no DSN coverage is needed for navigation. In reality, the comparison would not be as stark. A significant fraction of the tracking for the radiometric case, perhaps up to 50%, could probably be removed without changing the results significantly. For the optical case, some DSN time would still be necessary for periodic monitoring of spacecraft telemetry and to update on-board software and data sets.

Discussion

The InSight case study results demonstrate that the advantages and disadvantages of an on-board optical navigation system are mission-specific and require a more complete analysis than simply computing position uncertainty as a function of time. Generally, there are additional fuel costs and degraded delivery accuracy associated with an optical-only approach. On the other hand, the optical approach always reduces the DSN tracking needs and always allows for a later DCO, which can improved navigation performance significantly. If the technology development risk associated with the optical system were to be retired, the optimal mathematical solution for real missions would probably be some combination of ground-based radiometric tracking and on-board optical navigation. For a given mission, the analysis needs to be performed and relative benefits of each approach weighed carefully.

For the specific case of InSight, which is representative of a general Mars lander mission, the results in Table 4 show that the key requirement for the EFPA can only be met by an optical-only system if a high-quality camera system is implemented. Even then, the assumption that the Phobos and Deimos measurements can be made to an accuracy of 0.25 pixels would need to be proven for the case when those bodies are larger than 1-pixel in the image. The increase in $\Delta V99$ would also need to be evaluated against the spacecraft capabilities for the choice of camera. The results suggest that a lander mission might be able to benefit from an optical-only approach during the cruise phase, with some DSN tracking on the approach to Mars (including DDOR) to meet the EFPA requirement.

For a Mars orbiter mission, Fig. 5 indicates that the applicability of on-board optical navigation depends on the mission requirements. While the B-Plane delivery is less accurate than the radiometric approach with all but the best camera, it may still be acceptable when compared to mission requirements. For an orbiter mission, the ± 7 km B-Plane uncertainty associated with the Low Res camera would likely be insignificant compared to the maneuver execution on the orbit insertion burn. So long as the mission can accomodate the extra fuel needed (Table 5), the results here suggest that this approach would be quite feasible for a Mars orbiter mission (with the caveat that the late Phobos and Deimos measurement accuracy assumption should be revisited).

CONCLUSION

The results here consider the concept of using images of distant asteroids, planets, and moons as the fundamental measurement to enable an on-board spacecraft navigation system. This concept has been studied in the past and was actually demonstrated on-board NASA's Deep Space 1 spacecraft. Two significant new contributions are made: a characterization is presented of the position estimate accuracy that can be achieved throughout the solar system (as opposed to along a specific mission trajectory) and a detailed comparison of the performance of such a system against a radiometric navigation option for a real mission scenenario (the InSight mission) is performed.

The solar-system wide analysis here shows that the notion of triangulating spacecraft position based on images of distant bodies is mathematically feasible throughout the inner solar system with

even a relatively-basic space-rated camera that can see up to apparent magnitudes of 9.5. Using the planets, their large moons, and almost 50,000 well-known asteroids, it is shown that such a camera can typically see a couple dozen bodies anywhere inside of the outer edge of the main-asteroid belt. This capability is well more than the minimum of two bodies that are required to triangulate position, which lends robustness and the possibility for improved estimation accuracy. The kinematic position estimate accuracy is computed across the solar system for three different camera options and plotted. Under the assumptions used here, typical 1-σ triangulation uncertainties inside of the outer edge of the main-asteroid belt are 500-5000 km for a simple camera ($M \leq 9.5$), 200-1000 km for a mid-grade space-rated camera ($M \leq 10.5$), and 20-150 km for a high-quality science camera ($M \leq 13.5$), with the most accurate results occurring within the main belt. Outer solar system results are also presented, but the lack of targets at those distances results in significant degradation of accuracy and feasibility.

The on-board optical navigation paradigm is applied to the current plans for NASA's InSight mission and compared against the mission's baseline radiometric ground-navigation approach. The accuracy that the new approach can deliver the spacecraft to the Mars atmospheric entry and to the Mars B-Plane (a proxy for the orbit insertion location) is presented for three camera options. The increase in required fuel for trajectory corrections is also calculated. The exercise demonstrates the challenge associated with extrapolating orbit determination accuracy to mission feasibility and serves as a reminder to the reader that, ultimately, the applicability of the concept needs to be assessed in detail for any particular mission of interest. That said, if the results here are extrapolated, they suggest that an all-optical approach is likely a feasible option for most Mars orbiters, but additional radiometric measurement support might be necessary to achieve the navigation performance requirement for a Mars lander mission.

ACKNOWLEDGMENT

The authors would like to thank Eric Gustafson of the JPL InSight Navigation team for providing the MONTE setup files and technical support that enabled a thorough investigation of how an on-board optical navigation system would perform for that mission. They would also like to Troy Goodson of JPL for helping to interpret the $\Delta V99$ results. This work was performed at the Jet Propulsion Laboratory, California Institute of Technology, under contract with the National Aeronautics and Space Administration. Government sponsorship acknowledged.

NOTATION

Geometry

$\tilde{\mathbf{r}}_{sc}$	:	spacecraft position
$\tilde{\mathbf{r}}_b$	:	position of observation target 'b'
$\delta\tilde{\mathbf{r}}_b$	:	position of target 'b' relative to the spacecraft
δr_b	:	magnitude of $\delta\tilde{\mathbf{r}}_b$
$\delta\tilde{\mathbf{r}}_b^C$	:	$\delta\tilde{\mathbf{r}}_b$ in the camera frame $= \left[\delta\tilde{\mathbf{r}}_{b,x}^C, \delta\tilde{\mathbf{r}}_{b,y}^C, \delta\tilde{\mathbf{r}}_{b,z}^C\right]$
$\hat{\mathbf{\Delta}}_i$	:	unit vector of $\delta\tilde{\mathbf{r}}_t$
ϕ	:	Sun-target-S/C angle (a.k.a. phase angle)
ψ	:	Sun-S/C-target angle
θ	:	angle between two targets
$\mathbf{C}$	:	rotation matrix from inertial to camera frame
H	:	absolute magnitude
M	:	apparent magnitude

Target Sets

$\mathbf{T_{all}}$	:	set of all targets in database
$\mathbf{T_{visible}}$	:	set of visible targets
$\mathbf{T_{obs}^n}$	:	set of 'n' observed targets

Miscellaneous

t	:	time
$\mathbf{I}_{n\times n}$	:	$n \times n$ identity matrix

Filtering

n	:	number of observations considered
P_c	:	full kinematic covariance matrix
P_{xx}	:	kinematic position covariance
P_{cc}	:	consider parameter covariance
P_{xc}	:	cross-correlation between position and consider parameters
Λ	:	kinematic information matrix
Λ_b	:	kinematic information matrix contribution from observation of target b
$H_{x,b}$	:	partials of observable w.r.t. $\tilde{\mathbf{r}}_{sc}$
$H_{x,c}$	:	partials of observable w.r.t. $\tilde{\mathbf{r}}_b$
R	:	measurement covariance matrix
σ_{pos}	:	RSS of spacecraft position covariance
$\sigma_{pos,2}$	:	σ_{pos} with only two targets and no target position uncertainty

Camera and Image Processing Parameters

(s, l)	:	sample and line observables (pixels)
Θ	:	field-of-view of one camera pixel (a.k.a., IFOV)
M_{max}	:	maximum visible apparent magnitude
ψ_{min}	:	minimum allowable Sun-S/C-Target angle) angle for imaging
σ_{cf}	:	center-finding accuracy, 1-σ

APPENDIX A: DERIVATION OF 2-TARGET KINEMATIC POSITION-ESTIMATE ACCURACY

If only two targets are observed and the target ephemeris error is not considered, a closed-form solution for σ_{pos} can be derived. Under these assumptions, the covariance matrix in Eq. 5 simplifies to

$$\mathbf{P}_c = \mathbf{P}_{xx} = \left(\mathbf{H}_{x,1}^\top \mathbf{R}_1^{-1} \mathbf{H}_{x,1} + \mathbf{H}_{x,2}^\top \mathbf{R}_2^{-1} \mathbf{H}_{x,2}\right)^{-1} \tag{11}$$

For this derivation, the measurements are the unit vectors between the spacecraft and the target body, $\hat{\mathbf{\Delta}}_b$, instead of the sample and line camera coordinates.

$$\hat{\mathbf{\Delta}}_b = \left(\delta\tilde{\mathbf{r}}_b^\top \delta\tilde{\mathbf{r}}_b\right)^{-1/2} \delta\tilde{\mathbf{r}}_b \tag{12}$$

Without loss of generality, assume an inertial coordinate frame such that

$$\hat{\mathbf{\Delta}}_1 = \begin{bmatrix} 1 \\ 0 \\ 0 \end{bmatrix} \qquad \hat{\mathbf{\Delta}}_2 = \begin{bmatrix} \cos\theta \\ \sin\theta \\ 0 \end{bmatrix} \tag{13}$$

where θ is the angle between the two measurements. The measurement covariance matrices $\mathbf{R}_1$ and $\mathbf{R}_2$ are needed in the inertial coordinate frame. It is assumed that the target is along the $\hat{\mathbf{z}}$-direction

in the camera from, such that

$$\mathbf{R}_1 = \mathbf{R}_z(-\pi/2)\mathbf{R}_x(-\pi/2) \begin{bmatrix} \sigma_z^2, & 0, & 0 \\ 0, & (\Theta\sigma_{cf})^2, & 0 \\ 0, & 0, & (\Theta\sigma_{cf})^2 \end{bmatrix} \mathbf{R}_x^T(-\pi/2)\mathbf{R}_z^T(-\pi/2) \tag{14}$$

$$= \begin{bmatrix} (\Theta\sigma_{cf})^2, & 0, & 0 \\ 0, & (\Theta\sigma_{cf})^2, & 0 \\ 0, & 0, & \sigma_z^2 \end{bmatrix} \tag{15}$$

and

$$\mathbf{R}_2 = \mathbf{R}_z(-\pi/2-\theta)\mathbf{R}_x(-\pi/2) \begin{bmatrix} \sigma_z^2, & 0, & 0 \\ 0, & (\Theta\sigma_{cf})^2, & 0 \\ 0, & 0, & (\Theta\sigma_{cf})^2 \end{bmatrix} \mathbf{R}_x^T(-\pi/2)\mathbf{R}_z^T(-\pi/2-\theta) \tag{16}$$

$$= \begin{bmatrix} \sin^2(\theta)\left(\Theta\sigma_{cf}\right)^2 + \cos^2(\theta)\sigma_z^2, & \begin{pmatrix} -\sin(\theta)\cos(\theta)\left(\Theta\sigma_{cf}\right)^2 \\ +\sin(\theta)\cos(\theta)\sigma_z^2 \end{pmatrix}, & 0 \\ \begin{pmatrix} -\sin(\theta)\cos(\theta)\left(\Theta\sigma_{cf}\right)^2 \\ +\sin(\theta)\cos(\theta)\sigma_z^2 \end{pmatrix}, & \cos^2(\theta)\left(\Theta\sigma_{cf}\right)^2 + \sin^2(\theta)\sigma_z^2, & 0 \\ 0, & 0, & \left(\Theta\sigma_{cf}\right)^2 \end{bmatrix}, \tag{17}$$

where $\mathbf{R}_x$ is a rotation matrix around the $\hat{\mathbf{x}}$ axis, $\mathbf{R}_z$ is a rotation matrix around the $\hat{\mathbf{z}}$ axis, and σ_z is the uncertainty along the observation direction (which is ill-defined and cancels out).

For the unit-vector measurement, the Jacobian $\mathbf{H}_{x,b}$ for target body i is

$$\mathbf{H}_{x,b} = \frac{\partial\hat{\mathbf{\Delta}}_b}{\partial\tilde{\mathbf{r}}_{sc}} = \frac{\partial\hat{\mathbf{\Delta}}_b}{\partial\delta\tilde{\mathbf{r}}_b}\frac{\partial\delta\tilde{\mathbf{r}}_b}{\partial\tilde{\mathbf{r}}_{sc}} = -\frac{\partial\hat{\mathbf{\Delta}}_b}{\partial\delta\tilde{\mathbf{r}}_b}, \tag{18}$$

where

$$\frac{\partial\hat{\mathbf{\Delta}}_b}{\partial\delta\tilde{\mathbf{r}}_b} = \left(\delta\tilde{\mathbf{r}}_b^\top\delta\tilde{\mathbf{r}}_b\right)^{-1/2}\mathbf{I} - \frac{1}{2}\left[\left(\delta\tilde{\mathbf{r}}_b^\top\delta\tilde{\mathbf{r}}_b\right)^{-3/2}\left(\mathbf{I}\delta\tilde{\mathbf{r}}_b + \delta\tilde{\mathbf{r}}_b\mathbf{I}\right)\right]\delta\tilde{\mathbf{r}}_b^\top \tag{19}$$

$$= \frac{1}{\delta r_b}\mathbf{I} - \frac{1}{2\delta r_b^3}\left(\mathbf{I}\delta\tilde{\mathbf{r}}_b\delta\tilde{\mathbf{r}}_b^\top + \delta\tilde{\mathbf{r}}_b\mathbf{I}\delta\tilde{\mathbf{r}}_b^\top\right) \tag{20}$$

$$= \frac{1}{\delta r_b}\mathbf{I} - \frac{1}{\delta r_b^3}\delta\tilde{\mathbf{r}}_b\delta\tilde{\mathbf{r}}_b^\top \tag{21}$$

$$= \frac{1}{\delta r_b}\left(\mathbf{I} - \hat{\mathbf{\Delta}}_b\hat{\mathbf{\Delta}}_b^\top\right). \tag{22}$$

and $\delta r_b = ||\delta\tilde{\mathbf{r}}_b||$. Substituting in the measurement assumptions in Eq. (13) yields

$$\mathbf{H}_{x,1} = -\frac{1}{\delta r_1}\begin{bmatrix} 0, & 0, & 0 \\ 0, & 1, & 0 \\ 0, & 0, & 1 \end{bmatrix} \quad \text{and} \quad \mathbf{H}_{x,2} = -\frac{1}{\delta r_2}\begin{bmatrix} 1-\cos^2(\theta), & -\sin(\theta)\cos(\theta), & 0 \\ -\sin(\theta)\cos(\theta), & 1-\sin^2(\theta), & 0 \\ 0, & 0, & 1 \end{bmatrix}. \tag{23}$$

Substituting Eqs. (17) and (23) into (11) yields the position estimate covariance for two targets (without target ephemeris uncertainty).

$$\mathbf{P}_c = \left(\frac{1}{\delta r_2^2 \left(\Theta \sigma_{cf}\right)^2} \begin{bmatrix} (1-\cos(2\theta))/2, & -\sin(2\theta)/2, & 0 \\ -\sin(2\theta)/2, & \left(1+\cos(2\theta)+2\frac{\delta r_2^2}{\delta r_1^2}\right)/2, & 0 \\ 0, & 0, & 1+\frac{\delta r_2^2}{\delta r_1^2} \end{bmatrix} \right)^{-1} \tag{24}$$

$$= \left(\Theta \sigma_{cf}\right)^2 \begin{bmatrix} \frac{\delta r_1^2 - \delta r_1^2 \sin^2(\theta) + \delta r_2^2}{\sin^2(\theta)}, & \frac{\delta r_1^2 \sin(2\theta)}{1-\cos(2\theta)}, & 0 \\ \frac{\delta r_1^2 \sin(2\theta)}{1-\cos(2\theta)}, & \delta r_1^2, & 0 \\ 0, & 0, & \frac{\delta r_1^2 \delta r_2^2}{\delta r_1^2 + \delta r_2^2} \end{bmatrix} \tag{25}$$

The square-root of the trace of Eq. (25) then gives the RSS of the 2-observation position uncertainty (without target ephemeris error effects),

$$\sigma_{pos,2}\left(\delta r_1, \delta r_2, \theta, \Theta, \sigma_{cf}\right) = \frac{\sqrt{\delta r_1^4 + \delta r_1^2 \delta r_2^2 \sin^2(\theta) + 2\delta r_1^2 \delta r_2^2 + \delta r_2^4}}{\sin(\theta)\sqrt{\delta r_1^2 + \delta r_2^2}} \Theta \sigma_{cf}. \tag{26}$$

APPENDIX B: TARGET SELECTION HEURISTICS

Depending on spacecraft location and capabilities (i.e., M_{max}, ψ_{min}, etc.), there may be tens to hundreds of potential target bodies that are visible (Fig. 2). The development of heuristic methods to select which targets should be observed is vital as it quickly becomes a massive combinatorial problem to choose the n best observations to minimize σ_{pos} (Eq. (9)). If, for instance, 50 total targets are visible and the spacecraft can observe 10 targets during a navigation session, there exist over 10 billion unique combinations of target observations. Two methods are presented here to select which targets should be observed with less computational burden. Other methods have also been developed by the authors, with comparable performance to the methods given here.

Closest target strategy

The simplest heuristic is to choose targets to observe in order of their relative distance from the spacecraft. The closest target is chosen first, the next closest is chosen second, and so on. This heuristic is attractive because of its extreme simplicity: only simple vector offsets need to be computed and sorted for the navigation software to develop an image sequence.

Pseudo-target strategy

Another approach is to select the nth target using the 2-target σ_{pos} expression (Eq. (26)) to drive a greedy heuristic. The first two targets are chosen by exhaustively considering all possible combinations to minimize $\sigma_{pos,2}$,

$$\mathbf{T}_{obs}^2 = \underset{\{i,j\} \in \mathbf{T}_{visible} \times \mathbf{T}_{visible}}{\arg\min} \sigma_{pos,2}\left(\delta \tilde{\mathbf{r}}_i, \delta \tilde{\mathbf{r}}_j, \Theta, \sigma_{cf}\right) \tag{27}$$

To choose subsequent targets, a "pseudo-target", $\delta\bar{\tilde{r}}_{n-1}$, is computed to represent all previous targets based on the information matrix,

$$\delta\bar{\tilde{r}}_{n-1} = \sum_{b \in \mathbf{T}_{obs}^{n-1}} \frac{\delta r_b}{n-1} \hat{\mathbf{v}}_{max} \tag{28}$$

where $\hat{\mathbf{v}}_{max}$ is the eigenvector corresponding to the maximum eigenvalue of Λ for $\mathbf{T}_{obs}^{n-1}$ (Eq. (6)). Each potential target is then evaluated using Eq. (26) and the target resulting in the minimum $\sigma_{pos,2}$ is added to the observation set.

$$\mathbf{T}_{obs}^{n} = \mathbf{T}_{obs}^{n-1} \cup \underset{\{b\} \in \mathbf{T}_{visible} \notin \mathbf{T}_{obs}^{n-1}}{\arg\min} \sigma_{pos,2} \left(\delta\bar{\tilde{r}}_{n-1}, \delta\tilde{\mathbf{r}}_b \right) \tag{29}$$

For a database of t possible targets, if n targets are to be chosen, this heuristic results in a total of $(n-1)t - \frac{n(n-1)}{2}$ analytic $\sigma_{pos,2}$ evaluations after the initial closest target is chosen. For 50 potential targets, choosing the 10 targets to observe takes only 405 evaluations.

Heuristics Performance

Fig. 6 shows an example performance of the above heuristics when compared to an exhaustive search. For the case presented, both the "closest target" and "pseudo target" heuristics perform well compared with the exhaustive search. The loss in accuracy resulting from using a heuristic is very small, especially when the dramatic improvement in computation time is considered. This behavior is consistent across almost all of the cases investigated.

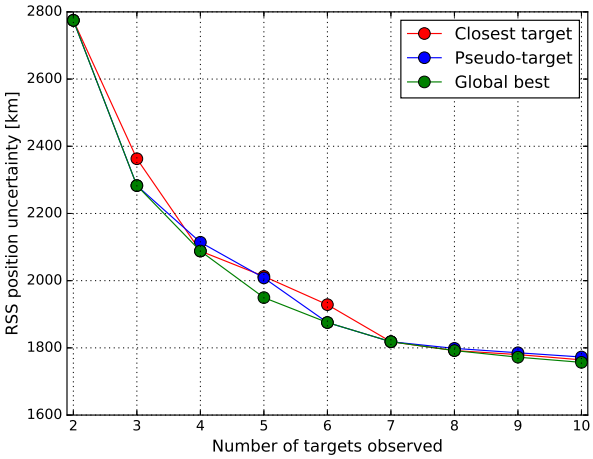

Figure 6. Comparison of σ_{pos} with different heuristics and number of targets. The spacecraft is placed at 1.5 AU along the J2000 Ecliptic $+X$ axis on July 31, 2016. Only asteroids are observed (not planets or moons). The Low Res camera option is used in these calculations.

The performance of the "closest target" heuristic is surprising given its simplicity. However, it does have a weakness in situations where the closest bodies may be very near to each other (for instance, on approach to Mars when Mars, Phobos, and Deimos are the three nearest targets). In these cases, variety in relative geometries of the targets is poor, resulting in σ_{pos} values that may be significantly worse than the exhautive best result. Still, for deep-space cruise with a wide distribution of possible targets, this heuristic performs well. For the "pseudo-target" heuristic, it approaches the global minimum σ_{pos} reliably and outperforms the "closest" heuristic in regions with a large concentration of potential targets within a small angular area of the sky. However, because it uses the analytic no-consider $\sigma_{pos,2}$ formulation to assess targets, it cannot discriminate between bodies with well known ephemerides and those that are more poorly known.

REFERENCES

[1] S. Bhaskaran, S. Desai, P. Dumont, B. Kennedy, G. Null, W. Owen Jr, J. Riedel, S. Synnott, and R. Werner, "Orbit Determination Performance Evaluation of the Deep Space 1 Autonomous Navigation System," *AAS/AIAA Spaceflight Mechanics Meeting, Monterey, CA*, 1998.

[2] S. Bhaskaran, J. Riedel, S. Synnott, and T. Wang, "The Deep Space 1 Autonomous Navigation System - A Post-Flight Analysis," *Astrodynamics Specialist Conference*, American Institute of Aeronautics and Astronautics, 2017/07/24 2000, doi:10.2514/6.2000-3935.

[3] J. Riedel, S. Bhaskaran, S. Desai, D. Han, B. Kennedy, T. McElrath, G. Null, M. Ryne, S. Synnott, T. Wang, *et al.*, "Using Autonomous Navigation for Interplanetary Missions: The Validation of Deep Space 1 AutoNav," *Fourth IAA International Conference on Low-Cost Planetary Missions*, No. L-0807, International Academy of Astronautics, 2000.

[4] "HORIZONS System," `https://ssd.jpl.nasa.gov/?horizons`. Accessed July 2017.

[5] D. G. Tuckness and S.-Y. Young, "Autonomous Navigation for Lunar Transfer," *Journal of Spacecraft and Rockets*, Vol. 32, No. 2, 1995, pp. 279–285.

[6] A. Long, D. Leung, D. Folta, and C. Gramling, "Autonomous Navigation of High-Earth Satellites using Celestial Objects and Doppler measurements," *Astrodynamics Specialist Conference*, 2000, p. 3937.

[7] M. Vasile, F. Sironi, and F. B. Zazzera, "Deep Space Autonomous Orbit Determination using CCD," *AIAA/AAS Astrodynamics Specialist Conference and Exhibit*, 2002, pp. 1–5.

[8] N. Ceccarelli, A. Garulli, A. Giannitrapani, M. Leomanni, and F. Scortecci, "Spacecraft Localization via Angle Measurements for Autonomous Navigation in Deep Space Missions," *IFAC Proceedings Volumes*, Vol. 40, No. 7, 2007, pp. 551–556.

[9] R. Zanetti, "Autonomous Mid-Course Navigation for Lunar Return," *Journal of Spacecraft and Rockets*, Vol. 46, No. 4, 2009, p. 865.

[10] J. V. Llop, "Autonomous Optical Navigation for Orbits around EarthMoon Collinear Libration Points," *Acta Astronautica*, Vol. 86, 2013, pp. 119 – 125, http://dx.doi.org/10.1016/j.actaastro.2013.01.007.

[11] Y. Kawabata, T. Saiki, and Y. Kawakatsu, "Simplified Covariance Estimation and Target Observation Management Method for On-Board Optical Navigation of Deep Space Probe," *International Symposium on Space Flight Dynamics*, No. ISSFD-2017-138, 2017.

[12] B. Segret, D. Hestroffer, G. Quinsac, M. Agnan, and J. Vannitsen, "On-Board Orbit Determination for a Deep Space CubeSat," *International Symposium on Space Flight Dynamics*, No. ISSFD-2017-122, 2017.

[13] "Index of /pub/naif/generic_kernels/spk," `https://naif.jpl.nasa.gov/pub/naif/generic_kernels/spk/`. Accessed July 2017.

[14] W. M. Owen Jr., "Methods of Optical Navigation," *Astrodynamics Specialist Conference*, No. 11-215, American Astronautical Society, 2011.

[15] B. Tapley, B. Schutz, and G. Born, *Statistical Orbit Determination*. Elsevier, 2004.

[16] L. Wood, "Interplanetary Navigation," *Encylopedia of Aerospace Engineering*, Vol. 5, John Wiley and Sons, Ltd., 2010, pp. 3071–3084.

[17] A. Halsell, "InSight Navigation Plan (2018 Baseline) Revision B," No. JPL D-75284, 2017.

[18] S. Evans, W. Taber, T. Drain, J. Smith, H. Wu, M. Guevara, R. Sunseri, and J. Evans, "MONTE: The Next Generation of Mission Design and Navigation Software," *The 6th International Conference on Astrodynamics Tools and Techniques*, 2016.

[19] E. Maize, "Linear Statistical Analysis of Maneuver Optimization Strategies," *AAS/AIAA Astrodynamics Specialist Conference, Kalispell, Montana*, 1987.

[20] W. Kizner, "A Method of Describing Miss Distances for Lunar and Interplanetary Trajectories," No. JPL External Publication No. 674, 1959.